

Processability, microstructure and precipitation of a Zr-modified 2618 aluminium alloy fabricated by laser powder bed fusion



Marvin Schuster^{a,b}, Anthony De Luca^a, Remo Widmer^a, Xavier Maeder^a,
Christian Leinenbach^{a,b,*}

^a Empa - Swiss Federal Laboratories for Materials Science and Technology, 8600 Dübendorf, Switzerland

^b École Polytechnique Fédérale de Lausanne (EPFL), Laboratory for Photonic Materials and Characterization, 1015 Lausanne, Switzerland

ARTICLE INFO

Article history:

Received 16 March 2022

Received in revised form 29 April 2022

Accepted 5 May 2022

Available online 7 May 2022

Keywords:

Laser powder bed fusion

SLM

2618

Processing

Precipitates

Microstructure

ABSTRACT

Additive manufacturing offers the opportunity to produce complex geometries from novel alloys with improved properties. Adapting conventional alloys to the process-specific properties can facilitate rapid implementation of these materials in industrial practice. Nevertheless, the processing of conventional alloys by laser powder bed fusion is challenging, particularly in cases of pronounced susceptibility to hot cracking.

Previous studies have demonstrated the positive influence of zirconium on the susceptibility to hot cracking of high-strength aluminum alloys, although its influence on precipitation formation, which is immensely important for 2xxx alloys, remains largely unexplored. This work investigates the optimum process parameters and precipitation formation of 2618 modified by zirconium in laser powder bed fusion.

The addition of zirconium results in the production of a crack-free, high-density (~99.9%) material. The microstructure is characterized by a trimodal grain size distribution. Very fine (~0.5 µm) equiaxed grains, nucleated by L1₂-Al₃Zr precipitation at the melt pool boundary, followed by columnar-dendritic grains (5–15 µm long, 1–3 µm wide) and coarser equiaxed grains (1–3 µm) form during solidification. The grain boundaries are populated predominantly by (Al,Cu)₉FeNi, but also by Mg₂Si, Al₂CuMg, and AlCu, which presumably impede grain growth and promote a very fine-grained, low-textured microstructure, even in regions where L1₂-Al₃Zr are absent. The as-built microhardness of 1360 ± 74 MPa exceeds that of the known high-strength Al alloys tailored to additive manufacturing, Addalloy™ and Scalma alloy®. The results provide a better understanding of precipitate formation in Zr-modified 2xxx series alloys and pave the way for the commercialization of further 2xxx alloys adapted to additive manufacturing.

© 2022 The Author(s). Published by Elsevier B.V.

CC-BY-NC-ND 4.0

1. Introduction

Metal additive manufacturing (AM) belongs to the group of generative manufacturing processes, which allow the tool-free production of complex metal parts. Among the different AM processes, the most widely used process is Laser Powder Bed Fusion (LPBF). Layer-by-layer, a near-net-shaped component is manufactured from metal powder using a focused laser beam. By selectively melting a thin layer of metal powder applied by a coater blade or roller onto a substrate or a metallurgically fused layer in a prior step, a three-dimensional component is formed [1,2].

While many alloy classes (steels, Ni, and Ti alloys) can be manufactured relatively reliably using LPBF, additive manufacturing of

high-strength Al alloys remains challenging. Although they offer low density and high specific strength, making them the ideal choice for the production of complex lightweight components, the material- and process-inherent characteristics coupled with an often insufficient understanding of its reciprocal influence, prevent their broader application. The usual problems encountered during AM of Al alloys are (i) porosity, (ii) hot cracks, (iii) strong crystallographic textures, (iv) and surface quality, the latter not being of interest for this work. (i) Possible causes for macropore formation are the selection of a too-large hatch distance between the melt tracks, gas inclusions, or moisture in the powder, as well as the balling effect, which results from capillary instabilities coupled with the poor wettability of solid and liquid Al melt. The main cause of the formation of macropores is the high reflectivity in the wavelength range of lasers typically used (Nd:YAG, fiber lasers), which, together with the high thermal conductivity, requires the use of high energy densities to liquefy Al alloys [3]. The fact that the absorption capacity

* Corresponding author at: Empa - Swiss Federal Laboratories for Materials Science and Technology, 8600 Dübendorf, Switzerland.

E-mail address: christian.leinenbach@empa.ch (C. Leinenbach).

increases strongly in the liquid state leads to high melt temperatures, which favor the evaporation of volatile alloying constituents, which are commonly added as solid solution strengtheners or precipitate-forming elements (e.g. Zn, Mg, Mn) [4]. The gas agglomerates and forms gas bubbles in the melt in the form of spherical pores due to surface tension. Due to the high cooling rate caused by the small melt pool volume and the high thermal conductivity, these pores become entrapped within the solidified material. The partial removal of these elements, coupled with the formation of pores, significantly reduces the mechanical performance of high-strength Al alloys. (ii) Elemental segregation in alloys with a large solidification interval creates a low melting point film on the grain boundaries (GB) and in the interdendritic region. Solidification shrinkage and thermal contraction cause tensile stress/strain on this film. If the viscosity of the melt is insufficient to backfill the resulting crevices, solidification cracks form, potentially spanning multiple layers [5]. High-strength Al alloys in particular are susceptible to hot cracking due to their large solidification interval and their alloying elements (especially Mg, Cu, and, in the case of small amounts, Si) [6,7]. (iii) A strong crystallographic texture results in an often undesirable directional dependence of the mechanical properties. Not only by selecting suitable process parameters [8–10] but also by using the right alloying elements [11,12], the anisotropy can be significantly reduced.

Despite these difficulties, (near-)eutectic Al-Si alloys (AlSi10Mg, AlSi12, etc.) can be produced very successfully by LPBF. Besides Si reduces the solidification interval and the melt viscosity, the wettability between molten and solidified alloy is increased, allowing a more efficient crack backfilling during solidification [13]. Furthermore, these alloys usually contain very few or no volatile alloying elements (like Mg), which could lead to pore formation in the process. By choosing an appropriate scan strategy, anisotropy can be greatly reduced as well [8]. However, while Al-Si alloys have been proven to be compatible with AM, they cannot be used in applications that require the high-strength aluminum class of alloys such as 2xxx, 5xxx, and 7xxx, as their mechanical properties are mediocre.

In recent years, the range of Al alloys has been complemented by high-strength alloys adapted to the unique process conditions in AM. The development of alloys containing Sc and/or Zr, a strategy that has long been used in casting technology is particularly noteworthy. Both elements form primary Al_3Zr (metastable) and Al_3Sc (stable) with an $\text{L}_{12}\text{-Al}_3\text{M}$ crystal structure. These Al_3M precipitates show more than 20 matching interfaces with aluminum, less than 0.52% lattice mismatch, and only a 1% difference in atomic density [5]. Thus, these precipitates can act as inoculation sites for the $\alpha\text{-Al}$ matrix formation and are extremely effective in inducing a fine, equiaxed microstructure. Due to the high mobility of the fine, equiaxed grains in the temperature range between liquidus and solidus temperature, stresses on the GB film can be relieved by translational and rotational motion of the grains. Hence, not only can the susceptibility to hot cracking be significantly reduced, but concurrently the grain refinement effect causes an increase in strength due to GB strengthening as well as in ductility due to a higher probability of adjacent grains with an orientation favorable for dislocation movement.

This mechanism was first demonstrated for AM by Martin et al. [5]. The two hot cracking susceptible 6061 and 7075 alloys could be manufactured crack-free and with an equiaxed microstructure. This was accomplished by ex-situ decoration of the feedstock powder with nm-sized hydrogen-stabilized Zr particles, which in-situ form Al_3Zr inoculation nuclei during melting of the powder. However, the process of coating the feedstock powders with nanoparticles is not trivial.

The well-known Sc and Zr modified 5xxx alloy Scalmalloy® (Al-4.5Mg-0.7Sc-0.35Zr plus additions of mainly Mn, Fe, and Si) take advantage of this mechanism. However, in contrast to the approach

used by Martin et al., no nm-sized powder is applied ex-situ to the powder particles, but instead, pre-alloyed powder is used to form $\text{L}_{12}\text{-Al}_3\text{M}$ precipitates [12]. This results in a crack-free duplex microstructure consisting of fine equiaxed grains and coarse columnar grains. The mechanical properties of this alloy are excellent, but the high price of the rare earth metal Sc prevents its more widespread use. A comparable microstructure of a 5xxx series alloy, but without the use of Sc, was obtained by Croteau et al. with the alloy marketed as Addalloy™ [11]. The base is an Al-4Mg alloy to which 1–2 wt% Zr is added. The advantage lies in the significantly lower price of Zr compared to Sc, with comparably good mechanical properties, making it an inexpensive and often suitable alternative to Scalmalloy®.

The positive effect on the reduction of hot cracking susceptibility due to grain refinement by the addition of $\text{L}_{12}\text{-Al}_3\text{M}$ precipitate forming elements has already been shown for other Al alloy classes [5,14]. Of particular note is the 2xxx series, with Cu and Mg as the main alloying elements. This alloy class is considered to be non-weldable due to its susceptibility to hot cracking, which makes its fabrication by AM extremely difficult [15,16]. Selected alloys of the 2xxx series could be fabricated crack-free without a change in chemical composition (e.g. 2022, 2024, 2219, 2618), albeit with a reduced processing window, cross-sections exhibiting high porosity or only specific geometries can be fabricated defect-free (i.e. building of wall structures, small part geometries) [17]. In recent studies, the positive effect of Zr addition on hot cracking susceptibility was also shown for 2xxx series alloys. Zhang et al. combined the feedstock powder (Al-4.24Cu-1.97Mg-0.56Mn) with μm -sized Zr powder by mechanical alloying and were able to fabricate a fine-grained microstructure with high density, good mechanical properties, and no cracking in a larger process window [18]. A similar approach was employed by Nie et al. who mixed Al-4.24Cu-1.97Mg-0.56Mn and μm -sized Zr powders and found an enlargement of the process window with increasing Zr content. The highest density was found for Zr contents of 2 wt% and slow scan velocities. However, such blended powders often exhibit inhomogeneity in the microstructure due to locally different chemical compositions, which is due to insufficient mixing of both powder grades [19]. Li et al. took this into account and investigated the effect of different Zr contents on the microstructure of a modified pre-alloyed 2024 (Al-4.40Cu-1.51Mg-1.15Mn-XZr, X = 0–3.72 wt%) [20]. A Zr content > 1.98 wt% is necessary for high density without cracks. All investigations have in common that they only focus on the grain size and the grain refinement inducing Al_3Zr precipitates. Furthermore, they lack a detailed characterization of the microstructure and the nature of the secondary phases. It is typically assumed that the phases that formed in AM consolidated parts are the same as in conventionally produced material, thus not considering the effects of fast cooling rates.

The modification of known alloys allows a smooth transition from traditional to generative manufacturing and bridges the gap towards the increased use of AM in industry. The 2618 alloy was chosen because of its susceptibility to hot cracking in LPBF, which has so far prevented its widespread technical application. The influence of rapid solidification in AM on microstructure and precipitate formation in 2xxx series alloys, in particular, is largely unexplored. The formation of metastable phases, as well as process-specific defects, must be understood in depth to optimize the alloy composition, the processing parameters, as well as to enhance the available alloy spectrum.

In this work, the consolidation behavior during LPBF as well as the microstructure and precipitate formation in a Zr-modified 2618 alloy in the as-fabricated state was investigated. A special emphasis was put on the change in secondary phases chemistry due to the AM processing.

Table 1

Chemical composition. Nominal composition of commercial and Zr-modified 2618 as well as ICP-OES measurement of the chemical composition for the as-received powder and after L-PBF consolidation.

	Al	Cu	Mg	Zr	Fe	Ni	Si	Ti	Zn	Sn
2618, nominal	Bal.	1.80–2.70	1.20–1.80	–	0.90–1.40	0.80–1.40	0.15–0.25	0.00–0.20	0.00–0.15	–
This work, nominal	Bal.	1.90–2.70	2.00–2.20	1.80–2.00	0.90–1.30	0.90–1.20	0.10–0.25	0.04–0.10	≤ 0.10	–
Powder, ICP-OES	Bal.	2.36 ± 0.10	1.95 ± 0.02	1.71 ± 0.05	1.17 ± 0.01	0.97 ± 0.01	0.24 ± 0.01	< 0.01	0.01 ± 0.001	0.05 ± 0.001
As-built, ICP-OES	Bal.	2.40 ± 0.09	1.55 ± 0.03	1.71 ± 0.05	1.18 ± 0.03	0.97 ± 0.02	0.23 ± 0.01	< 0.01	< 0.01	< 0.03

2. Materials and methods

2.1. Feedstock Powder

The Zr-modified 2618 powder was produced by ECKA Granules Germany GmbH with the nominal chemical composition given in Table 1. To determine the actual composition, the feedstock powder was analyzed by inductively coupled optical emission spectroscopy (ICP-OES). For that, the powder was dissolved with sodium hydroxide solution (40%) and neutralized with hydrochloric acid (37%). The sample was completely dissolved using a medium pressure microwave oven at 180 °C for 30 min and then analyzed using an Agilent 5110. The particle size distribution was determined by laser diffraction (Supplementary Figure 1) and has a d_{50} of 39.1 μm (d_{10} – d_{90} = 29.9–51.4 μm), showing a slightly right-skewed distribution with a noteworthy fraction of both fine (<20 μm) and coarse (>70 μm) particles. The bulk density of the powder according to EN ISO 3923/1 and the flow rate at a funnel size of 2.54 mm according to EN ISO 4490 is 1.38 g/cm³ and 65.5 s/50 g, respectively. The powder shows a predominantly spherical morphology with many satellite particles and splatters (Supplementary Figure 2). While no large entrapped porosity is observed in the powder cross-section, nanopores on GBs are occasionally present. Numerous primary Al₃Zr precipitates are evident within the predominantly equiaxed grains. A eutectic phase on the GBs is also evidenced.

2.2. Laser powder bed fusion

The LPBF experiments were performed on a Sisma MySint 100, which is equipped with a 1070 nm Yb fiber laser, enabling a maximum laser power of 200 W at a spot size of 55 μm . During the build jobs, Ar 4.6 shielding gas (99.996%) was used at atmospheric pressure to keep the oxygen concentration in the build chamber below 100 ppm O₂. The components were fabricated on a build platform of AlSi10Mg with a diameter of 100 mm and subsequently cut by electro-discharge machining (EDM). Since 2xxx series alloys are known for their natural aging behavior when exposed to room temperature, the samples were stored in the freezer at –26 °C between each preparation and characterization step. A design of experiments was developed to determine the influence of the manufacturing parameters (laser power, scan speed, and hatch distance) and to optimize these parameters for the resulting part density. The circumscribed central composite design (CCD) allows a reduction of the number of specimens without loss of information [21]. For this purpose, twenty cubic 10×10×10 mm³ specimens were fabricated in the following parameter space: Laser power of 113–197 W, scan speed of 149–401 mm/s, and hatch distance of 0.083–1.117 mm. Layer thickness was fixed at 0.03 mm. A bidirectional scanning strategy with 90° rotation between layers was chosen. By eliminating non-significant terms based on a significance level of α = 15% and then optimizing the response variable density of the quadratic model with interactions, the following parameter set was obtained and employed for all conducted experiments: Laser power 168 W, scan speed 149 mm/s and hatch distance 0.1168 mm.

2.3. Microstructure characterization

The densities of the consolidated parts were measured using Archimedes' principle in ethanol. The theoretical density of the alloy at room temperature was estimated at 2.80 g/cm³ by using Thermo-Calc® 2021 with the TCAL6 database. Based on this, we only give the relative density of the manufactured samples. Subsequently, the specimens were cut up parallel to the build direction using a precision cutting machine and cold mounted in epoxy resin. This was followed by grinding with #2500 grit abrasive paper and polishing with 6 μm and 1 μm diamond suspension. The final polishing step was performed using a 50 nm colloidal silica solution.

Microhardness measurements were conducted on a Fischerscope HM2000 hardness tester. A load of 2000 mN, for an indentation time of 5 s, was employed. The reported microhardness values correspond to the average of at least ten measurement points per sample.

The microstructure was analyzed using scanning electron microscopy (SEM) on both an FEI NanoSEM 230 and an FEI Quanta 650 FEG, equipped with a backscatter electron detector (BSD) for Z-contrast imaging. The chemical analysis was performed using energy-dispersive X-ray spectroscopy (EDX) detectors from Oxford Instruments and Thermo Fisher. The electron acceleration voltage for all SEM investigations was 12 kV. The texture analysis was conducted on a Tescan Mira using electron backscatter diffraction (EBSD). The polished sample was tilted at a surface angle of 70° and the SEM conditions for EBSD mapping were 20 kV acceleration voltage at 10 nA. The step size was 150 nm. The phase analysis was performed by X-ray diffraction (XRD) on a Bruker D8 diffractometer with Cu K α radiation, equipped with a 0.012 mm thick Ni filter.

For scanning transmission electron microscopy (STEM), lamellae were extracted perpendicular to the build direction using an FEI Helios NanoLab 600i focused ion beam (FIB). STEM was performed on an FEI Titan Themis microscope, equipped with a probe spherical aberration corrector. The acceleration voltage for the electron beam was 300 kV and a 25 mrad probe convergence semiangle was used. STEM imaging was done using a high angle annular dark-field (HAADF) detector with a 53 mrad inner/200 mrad outer collection semiangle. Chemical analysis was performed with the SuperEDX system (ChemiSTEM technology) with four silicon drift detectors for energy-dispersive X-ray spectroscopy (EDX). The phase analysis used the Al-K, Mg-K, Cu-L, Fe-L, Ni-L, Si-K, Sn-L, O-K and Zr-K lines and was conducted using Velox 3.0. Due to a high background level in the O signal, the reported quantification for all other elements was done without considering O. The reported O map was done counting all elements. To improve the counting statistic per pixel, a pre-filtering was applied. All TEM imaging was done with the build direction being out of the plane.

3. Calphad-assisted specification of alloy composition

The nominal chemical composition was determined based on literature in conjunction with computational thermodynamic modeling by Thermo-Calc® 2021 with the TCAL6 database. This work is derived from our previous investigations on a 2xxx series model alloy, which examined the influence of Zr addition on the consolidation and precipitation behavior of a 2xxx series model Al-Cu-

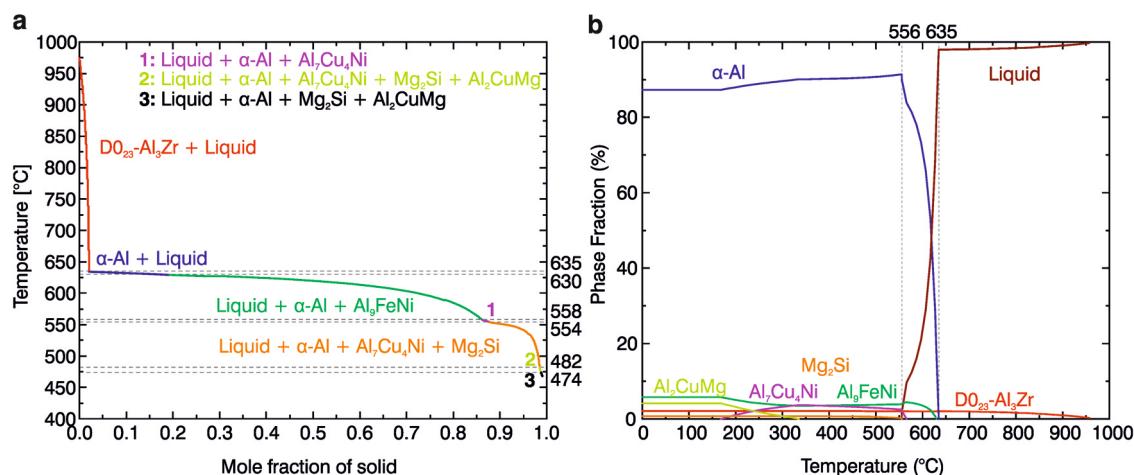


Fig. 1. Phases according to Thermo-Calc®. The chemical composition applied corresponds to the actual powder composition, Table 1. a) Scheil-Gulliver model predicts the formation of $\text{D}_{023}\text{-Al}_3\text{Zr}$ before the formation of the matrix (α -Al), followed by a high proportion of 67 mol.% Al_5FeNi + α -Al. During solidification of the remaining 15 mol.% liquid, smaller volume fractions of various precipitates form. b) Phase fraction simulations show the high-temperature stability of the Al_3Zr as well as the Al_5FeNi phase, exceeding the alloy's solidus temperature.

Mg-Zr alloy [22]. The processing of the present Zr-modified 2618 is, however, characterized by a much more complex precipitation sequence, as the different chemical composition and the correlation of precipitate formation with segregation effects during rapid solidification can often lead to the formation of unexpected phases with hitherto not reported chemical compositions. For the subsequent elaboration of tailored heat treatments (e.g. for an effective solutionizing of the material), these effects must be comprehensively understood.

When designing an alloy, it is imperative to consider both the extreme process conditions of the LPBF process, such as high temperatures of the melt, far-from-equilibrium solidification, the formation of metastable phases induced by rapid cooling rates above 10^7 K/s [23], and the material-inherent properties of Al alloys. The high reflectivity to the laser wavelengths typically used in LPBF (Nd:YAG and fiber lasers) as well as the high thermal conductivity of Al alloys requires the use of high energy densities to provide enough energy to melt the powder. This can lead to the vaporization of volatile alloying elements of the alloy, such as Mg or Zn. The resulting gas can become entrapped in the material during solidification and manifest as spherical gas pores due to surface tension [4]. Owing to the presence of a significant amount of Mg in 2618, its unavoidable vaporization must be taken into account during alloy design. To compensate for the evaporation and sublimation of Mg during processing, the Mg content of the raw powder alloy under investigation is 0.4–0.8 wt% higher than that of conventional 2618, at 2.0–2.2 wt% compared with 1.2–1.8 wt%. Previous investigations of the Mg-rich alloys Addalloy™ (3.7 wt% Mg) and AlCuMgZr (4.0 wt% Mg) showed Mg losses of 0.9 wt% and 0.7 wt%, respectively [11,22]. The appropriate choice of an Mg content in the feedstock powder thus allows the Mg content in the as-built part to conform to the nominal content in 2618.

Thermo-Calc® calculations based on the Scheil-Gulliver model and phase fraction simulations are depicted in Fig. 1. The Scheil-Gulliver calculations show the formation of the stable $\text{D}_{023}\text{-Al}_3\text{Zr}$ phase from 975 °C to 635 °C of up to 3.1 wt%, although the metastable L_{12} phase instead of the stable D_{023} phase is expected to form peritectically in the still-liquid melt due to the high cooling rates [11]. While the formation of the Al_3Zr phase starts at higher temperatures with increasing Zr contents, the consolidation of the matrix phase during cooling is independent of the Zr content. It is worth mentioning that the solidification interval shows a slight linear dependence of the magnesium content; the higher the

magnesium content, the earlier the solidification of the Al_3Zr phase starts and the later it ends. Additionally, $\text{L}_{12}\text{-Al}_3\text{Zr}$ nanoprecipitates can form from the Zr supersaturated matrix, which provide an additional source of strength alongside the typical S- Al_2CuMg phase formed during heat treatment of 2618. This dual precipitation strengthening by $\text{L}_{12}\text{-Al}_3\text{Zr}$ and S- Al_2CuMg was demonstrated on a simple quaternary AlCuMgZr base alloy [22].

The α -Al matrix phase forms in the range of 635–468 °C. All phases forming posterior to the matrix are presumably located on GBs due to elemental segregation. The subsequent formation of the Al_5FeNi phase forming in the range of 630–558 °C of up to 4.5 wt% is following literature and leads to a depletion of the Fe in the melt and concurrently to a proportional increase with Mg, Si, Ni, and Cu up to a solid phase fraction of 85 mol.% [24]. The resulting melt composition leads to the formation of 3.9 wt% $\text{Al}_7\text{Cu}_4\text{Ni}$ in the range 558–474 °C, which was also predicted by Hu et al. for the solidification of 2618 according to the Scheil model [24]. Since the Scheil model assumes a homogeneous element distribution in front of the solidification front, which often does not prevail, and the fraction of precipitates forming in the following is small, the prediction of the phases forming at this stage is challenging. While the formation of $\text{Al}_7\text{Cu}_2\text{Fe}$ was reported as a eutectic phase in Al-Cu-Fe-Si systems, it is not calculated by Thermo-Calc® [24]. In the further course of solidification in the range of 554–468 °C, the formation of Mg-rich phases, Mg_2Si and Al_2CuMg , is identified. This is due to the increase of Mg in the liquid until up to 25 wt%. While the formation of Mg_2Si is predicted first, Al_2CuMg joins in at 482 °C, leading to 0.6 wt% and 0.4 wt%, respectively [101]. While Hu et al. do not predict Al_2CuMg , its formation is observed by Belov et al. [24,25]. The phase fraction simulations show a liquidus temperature of 635 °C and a solidus temperature of 556 °C, exhibiting a narrower solidification interval than the experimentally determined temperatures of 647 °C and 541 °C for liquidus and solidus, respectively, Supplementary Figure 3, indicating the presence of non-predicted phases and/or the absence of certain phases. In general, as Hu et al. point out, the prediction of the microstructure via Thermo-Calc® for 2xxx series alloys is subjected to a high degree of uncertainty based on incomplete phase equilibrium data and the complex solidification sequence. Thus, the Thermo-Calc® results can solely serve as rough guidance and experimental results must confirm the calculations.

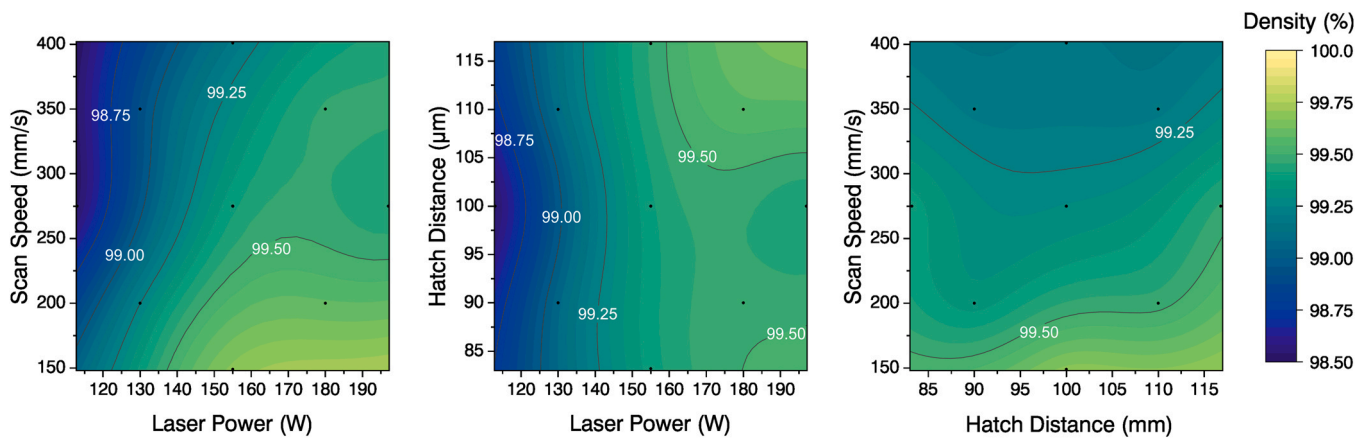


Fig. 2. Design of Experiments. The higher the values for laser power and hatch distance and the lower the values of scan speed, which is equivalent to a high energy density, lead to a high part density. The greatest influence on density comes in descending order from the laser power, followed by scan speed and hatch distance. However, all three factors are significant for a significance level of $\alpha = 15\%$. The dots represent the investigated consolidation parameter.

4. Results

4.1. Design of experiments

The influence of the investigated factors (scan speed, laser power, and hatch distance) on the measured relative density is depicted in the contour plots in Fig. 2. The dots represented the experimental data points, with the remaining field being extrapolated. Three types of models were examined for their suitability to explain the measured density values of the parameter survey: a linear model, a linear model with interactions, and a quadratic model with interactions. The quadratic model showed the highest R^2_{adj} of 94.42% and R^2_{pred} of 90.00% as well as the lowest *lack-of-fit*, which is why it was chosen for parameter optimization and prediction. R^2_{adj} allows an assessment of the *explained* variance to the total variance of a regression model and are independent of the number of model constants contained, R^2_{pred} gives information about the predictive capabilities of the model. By maximizing the regression model equation after stepwise elimination of non-significant factors at a significance level of $\alpha = 15\%$, the parameter combination of laser power, scan speed, and hatch distance to achieve highly-dense samples was determined as 168 W, 149 mm/s, and 0.11 mm, respectively. The trend towards higher density at comparatively high laser power and hatch distance as well as at low scan speed in the area of the investigated parameter space is evident. The highest influence on the density is exerted in descending order by laser power, followed by scan speed and finally hatch distance. While the values for laser power and hatch distance are within the parameter space considered, the optimum value of scan speed represents a minimum of the parameter space investigated. This indicates that with a further reduction of the scan speed, a shift from local to a possible global density maximum could be achieved. The density of all samples of the parameter study was above 99.5%. The relative density measured by Archimedes' principle density measurement for the determined optimal parameter combination was $99.93 \pm 0.02\%$, which is within the 95% confidence interval of the predicted value from the regression model of $99.90 \pm 0.06\%$.

4.2. Microstructure

Microstructural investigations were conducted on cross-sections parallel to the build direction, Fig. 3. A small area fraction of 10–25 μm circular pores was observed, randomly located in the part, Supplementary Figure 4. The individual melt pools, which are decorated by a eutectic/GB Fe-Ni-Cu-rich film, Fig. 3a, can be identified thanks to the change in grain size from edge to center of each track.

The width of the melt pools is in the range of 150–200 μm , with a depth of 100–150 μm . The microstructure shows a trimodal solidification morphology, Fig. 3b, with a change in solidification mode between each region: (i) the outer boundary of the melt pools, which solidifies first in the temporal course, consists of a 5–20 μm thick band of very fine, $\sim 0.5 \mu\text{m}$ -sized equiaxed grains. Square, Zr-rich bright precipitates of about 50–100 nm are very often visible in the grain centers; (ii) a band of 5–15 μm long and 1–3 μm wide columnar-dendritic, epitaxially grown grains from the fine-grains, (iii) in the further course of solidification, a strongly pronounced transition to a third solidification morphology can be observed, which consists of 1–3 μm -sized, equiaxed grains. The Zr-rich precipitates can be solely seen within the fine grains at the melt pool boundaries but not in later solidified regions.

At higher magnifications, a very low fraction of 100–500 nm diameter nanopores can be observed, typically located at GBs, in-between the Fe-Ni-Cu-rich eutectic film, Fig. 3c. These pores potentially arise either from the inability of the eutectic phase to backfill into pores or the presence of a low melting eutectic phase in the heat-affected zone (HAZ) of the following melt track. Thanks to the very fine grain structure, these nanopores do not act as a site for crack initiation and propagation. It should be particularly emphasized that no cracks were found in any of the samples examined in this work, regardless of processing parameters.

The EBSD mapping allows to more clearly identify the grain size distribution, Fig. 3d. While selected melt track boundaries can be clearly determined, the grain structure is overall rather irregular. For example, bands of fine grains can be found within the center of a melt track. The grain size is estimated to be in between 0.3 and 1.6 μm , with the largest area fraction of grains smaller than 0.5 μm located in the equiaxed region, which is responsible for the weak < 101 > texture in build direction, Fig. 3e. The microhardness in the as-built state averages $1360 \pm 74 \text{ MPa}$ with an indentation modulus of $94 \pm 3 \text{ GPa}$.

4.3. Phase identification

The phase identification, quantification as well as determination of the lattice parameters was performed by XRD, comparing the measured X-ray diffraction pattern with a calculated pattern refined by the Rietveld method, Fig. 4, Table 2. A large number of calculated phases show high agreement with the observed X-ray diffraction pattern. Besides the Al matrix phase (84.0 wt%), where the < 111 > and < 200 > peaks are recognizable, the Al_9FeNi phase occurs most frequently (11.2 wt%). Moreover, the stable $\text{D}_{023}\text{-Al}_3\text{Zr}$ phase (3.9 wt %) and the metastable counterpart $\text{L}_{12}\text{-Al}_3\text{Zr}$ (0.2 wt%) can be

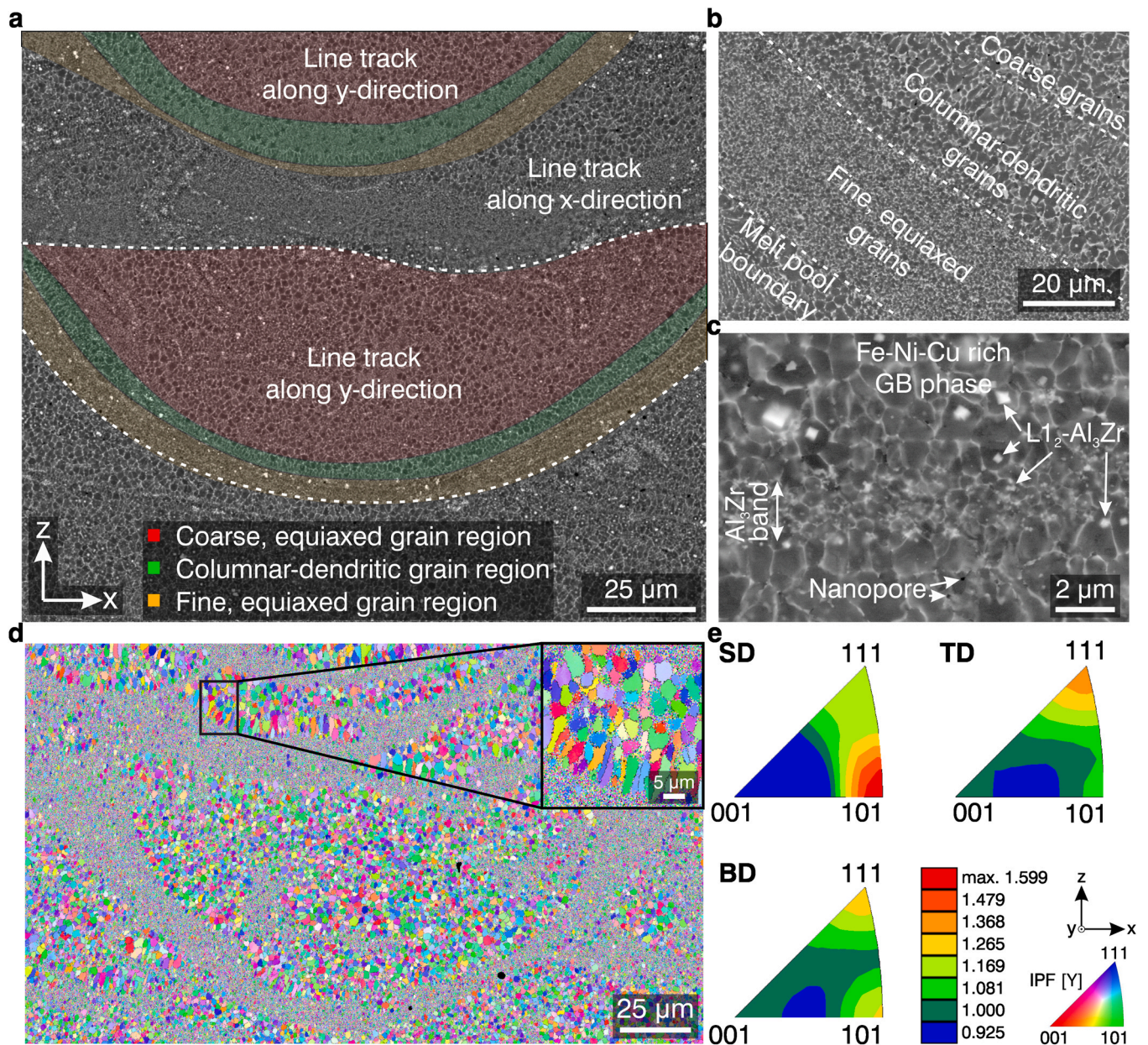


Fig. 3. As-built microstructure analysis by SEM-BSD and texture by EBSD. a) By 90° rotation of the scan direction between layers, melt tracks are oriented alternately parallel to the x- and y-direction. Three different solidification morphologies are discernible within melt pools. Z-direction corresponds to the build direction and applies to all sub-figures. b) At the edge of the melt pools are thin, 5–20 μm thick layers of very fine, equiaxed grains, followed by coarser, columnar-dendritic grains. c) Melt pool edge is characterized by an Al₃Zr band. GBs are occupied by a eutectic Fe-Ni-Cu rich phase. Nanopores are occasionally found on GBs. d, e) Melt pools show weak < 101 > texture in build direction (BD). The different melt pool regions are distinctly visible in the enlarged image section.

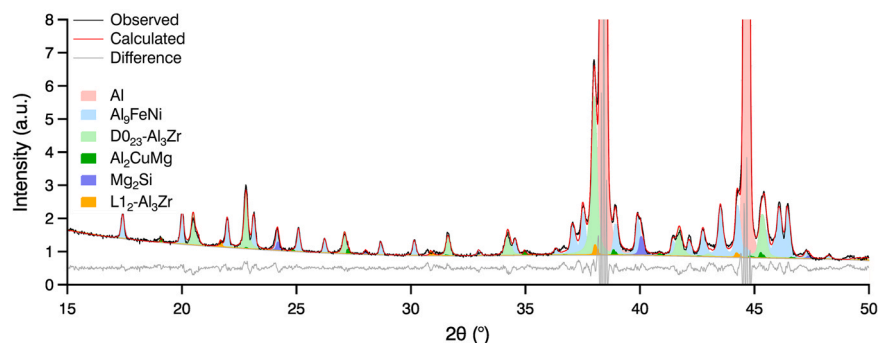


Fig. 4. XRD measurement. Phase identification by comparing the observations with Rietveld refined calculations.

Table 2

XRD phase quantification and lattice parameter identification. Phase fraction is quantified based on the relative peak intensities. Lattice parameters are evaluated using the Bragg equation.

Phase	Space group	Phase fraction (wt%)	a [Å]	b [Å]	c [Å]
α -Al	F m $\bar{3}$ m	84.0	4.06		
Al_9FeNi	P 1 2 ₁ /c 1	11.2	6.24	6.31	8.60
$\text{D}_{023}\text{-Al}_3\text{Zr}$	I 4/m m m	3.9	4.00		17.30
$\text{L}_{12}\text{-Al}_3\text{Zr}$	P m $\bar{3}$ m	0.2	4.09		
Mg_2Si	F m $\bar{3}$ m	0.5	6.36		
Al_2CuMg	C m c m	0.2	4.00	9.29	7.15

detected, [Supplementary Figure 4](#). Furthermore, Mg_2Si (0.5 wt%) and Al_2CuMg (0.2 wt%) can be identified. The lattice parameters determined in each case, whose accuracy depends on the corresponding evaluated mass fraction, are listed in [Table 2](#).

For phase confirmation and determination of the chemical distribution, STEM-HAADF and EDS mapping were performed on a FIB lamella sampled perpendicular to the build direction, [Fig. 5](#). A band of 50–75 nm Al_3Zr cubes was found to cross the region of interest. It is thus suspected that the investigated area corresponds to a melt pool boundary perpendicular to the build direction. Based on the curvature of the Zr-rich band, the regions below and above are identified as the heat affect zone (HAZ) and the remelted region of the melt pool. Due to the nucleation of α -Al on primary Al_3Zr , the grain structure is extremely fine (\varnothing 150–400 nm) in this band, [Fig. 6a](#). In the HAZ, the grains are large (up to 2 μm), while the remelted regions exhibit elongated grains perpendicular to the melt pool boundary. The GBs are populated in all areas of the melt pool by a eutectic phase containing Fe, Ni, and Cu at an approximately equiatomic ratio. The morphology of this phase varies depending on the area of the melt pool considered. In the HAZ and at the melt pool boundary, the eutectic forms a semi-continuous phase along GBs and in the interdendritic regions of larger grains, [Fig. 6b,c](#). In the remelted zone, the eutectic regions contain a high fraction of small, agglomerated globular eutectic phases. The two phases are, however, expected to be of the same type. Additionally, other compounds are

found alongside the eutectic phase: i) 30–50 nm binary Al-Cu-rich phase, ii) 50–250 nm Mg-Si-rich particles, iii) 25–150 nm Mg-O-rich dispersoids. No ternary Al-Cu-Mg-rich phases were detected in the investigated area, confirming that Al_2CuMg , observed by XRD is potentially present in a very low fraction, or localized in a certain region of the melt pool. Due to the low mass density of the two Mg-rich phases, they appear darker than the matrix. To differentiate them from pores, their shape, estimated from the EDS map, is outlined on the respective HAADF images.

Higher magnification EDS mapping was conducted in the thinnest area of the FIB lamellae, [Fig. 7](#), where overlap between the Al matrix and the secondary phases is reduced. Composition estimation of the Mg-Si rich phase shows a near-zero level of Al. The Mg-Si-rich and Al-Cu-rich phases are identified as Mg_2Si and CuAl, respectively, based on EDS composition and the identification of the FFT pattern, [Fig. 7c,d](#). As a confirmation of the phase identification, Al_2Cu was not a successful candidate for the binary Al-Cu phase, as the potential zone axis contained forbidden reflections that are observed in the experimental pattern. Around 1.5 at% Sn was observed in solution within in the Mg_2Si phase. In the HAZ, a small fraction of elongated $\text{L}_{12}\text{-Al}_3\text{Zr}$ precipitates was detected close or at the interface of other secondary phases (cf. Zr map in [Fig. 7](#)). The composition of the Mg-O-rich dispersoid could not accurately be measured due to the overlap with other phases. It is, however, suspected to be spinel MgAl_2O_4 , which is often found in other additively manufactured Al-Mg-based alloys [11,22,26].

The quaternary Al-Fe-Ni-Cu-rich phase has an estimated composition of $\text{Al}_{69}\text{Fe}_{11}\text{Ni}_9\text{Cu}_{11}$ (± 1 at%). However, no quaternary phases have been reported in the literature for this system [27]. For the measured composition, the closest ternary phases are $\text{Al}_7\text{Cu}_2\text{Fe}$ and Al_9FeNi . Both phases are likely candidates in terms of composition, if Ni occupies the Cu sublattice in $\text{Al}_7(\text{Cu,Ni})_2\text{Fe}$ or if Cu occupies the Al sublattice in $(\text{Al,Cu})_9\text{FeNi}$. A solubility of 4.5 at% Ni at 530 °C was reported for $\text{Al}_7\text{Cu}_4\text{Fe}$, which could also apply for the detected phase [24]. The analysis of the two-zone axis observed for this phase, [Fig. 7a,b](#), was conducted with the associated details in [Table 3](#). The experimental zone axes could fit both phases with

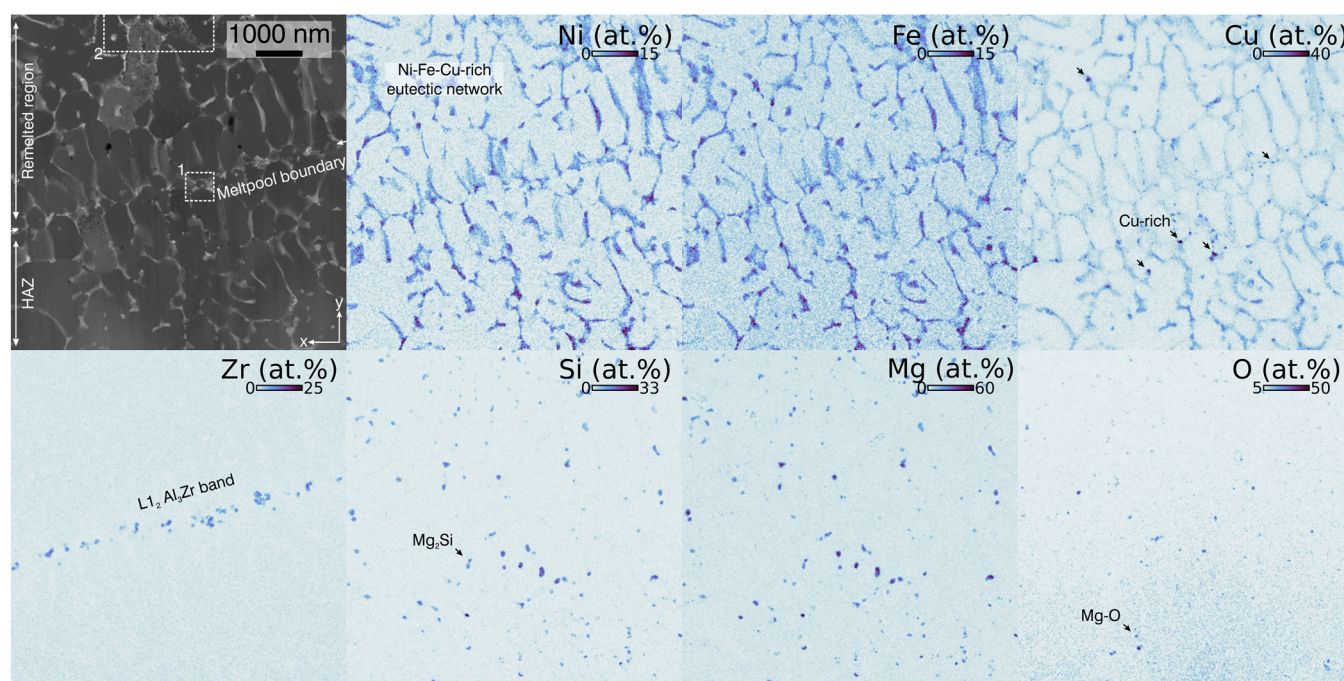


Fig. 5. STEM-EDS mapping of the area around a melt pool boundary. The melt pool boundary is identified by a thin band of $\text{L}_{12}\text{-Al}_3\text{Zr}$ cuboids. Based on the curvature of this band, the HAZ and remelted regions are identified. A eutectic network of Al-Ni-Fe-Cu-rich phase propagate through the microstructure, as well as a few binary Al-Cu phases. Increased Mg concentration is only found collocated with Si or O.

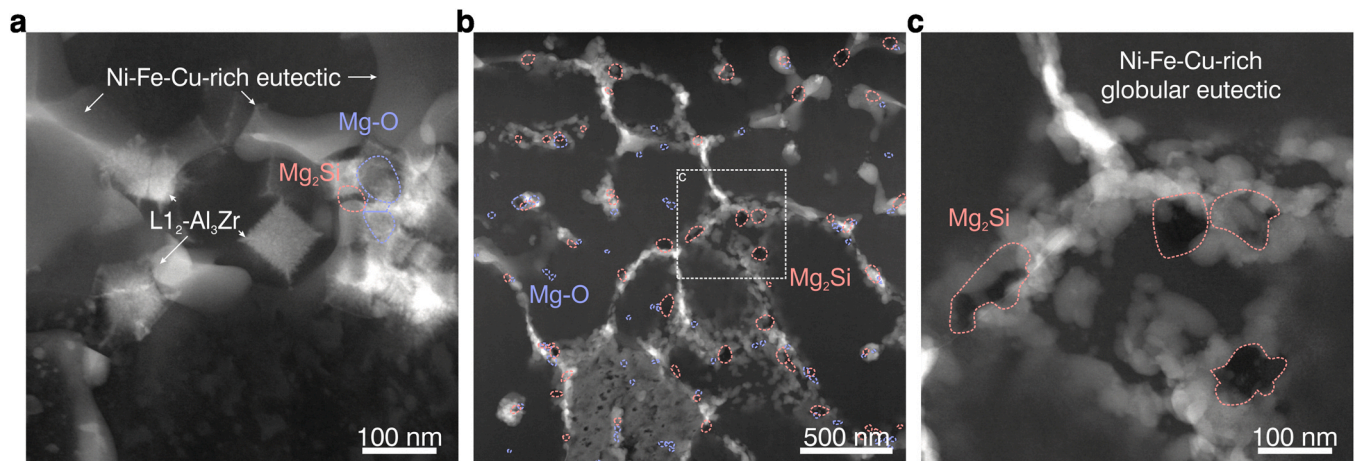


Fig. 6. STEM-HAADF imaging of a) the melt pool boundary, exhibiting primary cuboids $L1_2\text{-Al}_3\text{Zr}$, and b, c) the eutectic structure in the remelted region, exhibiting a "globular" shape. Due to the "black Z-contrast" of Mg_2Si and Mg-O , these phases were outlined based on the associated EDS mapping to differentiate from potential nano porosity. Region a and b correspond to regions 1 and 2, respectively, in Fig. 5.

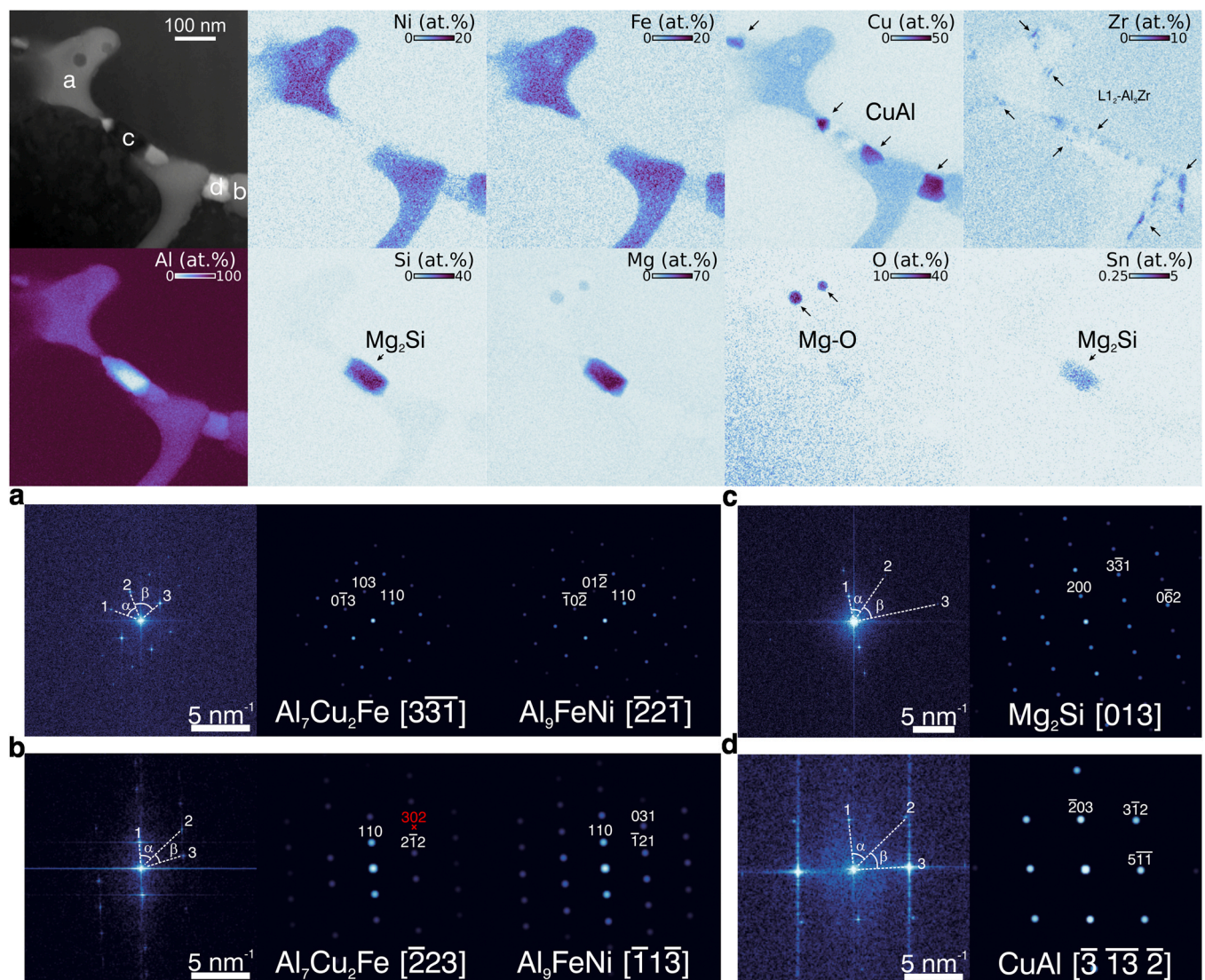


Fig. 7. Phase identification, conducted in the HAZ. EDS maps reveal the composition of the various phases observed in the system. Nanometric $L1_2\text{-Al}_3\text{Zr}$ are also observed at the boundary of the eutectic phases. The FFT patterns labeled a) to d) were acquired in the associated area on the STEM-HAADF image and compared to simulated zone axes of their respective phases. The reflection indicated in red in b indicates a forbidden reflection.

Table 3

STEM phase identification and interspacing measurements. The value in parenthesis indicates the deviation between experimental and theoretical values. Note: As the FFT analyses are conducted on a STEM micrograph, a certain "shearing" of the pattern is expected to increase the experimental errors for distances and angles.

Region	Pattern	Space group	d_1 [Å]	d_2 [Å]	d_3 [Å]	α [°]	β [°]
a	Exp		3.67 ± 0.01	3.82 ± 0.01	4.54 ± 0.01	48.7	68.2
	$\text{Al}_7\text{Cu}_2\text{Fe}$ [3 $\bar{3}$ 1]	P 4/m n c	3.8928 (+6.1%)	3.8928 (+1.9%)	4.4760 (−1.4%)	51.6 (+2.9°)	64.2 (−4°)
	Al_9FeNi [221]	P 1 2 ₁ /c 1	3.54158 (−3.5%)	3.6836 (−3.6%)	4.2444 (−2.5%)	48.2 (−0.5°)	68.5 (+0.3)
b	Exp		4.47 ± 0.02	2.05 ± 0.16	2.66 ± 0.27	49.1	26.8
	$\text{Al}_7\text{Cu}_2\text{Fe}$ [223]	P 4/m n c	4.4760 (+0.1%)	2.0292 (−1%)	2.6442 (−0.6%)	47.2 (−1.9°)	25.7 (−1.1°)
	Al_9FeNi [1 $\bar{1}$ 3]	P 1 2 ₁ /c 1	4.4244 (−1%)	2.0394 (−0.5%)	2.7021 (+1.6%)	47.8 (−1.3°)	26 (−0.8°)
c	Exp		3.19 ± 0.01	1.47 ± 0.01	0.98 ± 0.01	45.7	43.9
	Mg_2Si [013]	F m $\bar{3}$ m	3.1755 (−0.5%)	1.4570 (−0.9%)	1.0042 (+2.5%)	46.5 (+0.8°)	43.5 (−0.4°)
d	Exp		2.34 ± 0.01	1.59 ± 0.01	2.10 ± 0.01	49.9	42.5
	CuAl [$\bar{3}$ 1 $\bar{3}$ 2]	C 2/m	2.2443 (−4.1%)	1.5838 (−0.4%)	2.0249 (−3.6%)	51.1 (+1.2°)	44.6 (+2.1°)

reasonable agreement, preventing a selection of absolute certainty between the two phases. However, the $(\text{Al,Cu})_9\text{FeNi}$ patterns fit the experimental FFT more accurately. In region a, the angle difference is small, with the measured interplanar spacings being increased by ~3%, suggesting an increase of the lattice parameter due to Cu solubility. In region b, while the identified $\text{Al}_7\text{Cu}_2\text{Fe}$ zone axis fits the experimental patterns, some of the observed reflections should be forbidden. Based on these observations, $(\text{Al,Cu})_9\text{FeNi}$ is identified as the likely candidate for this quaternary phase, which is also quantified to represent a phase fraction of 11 wt% according to the XRD analysis.

5. Discussion

5.1. Processability and defects

Every sample in the parametric study shows a relative density higher than 99.5%, underlining the excellent processability of the alloy developed. Nevertheless, the effect of the parameters laser power, scan speed, and hatch distance on density is significant at $\alpha = 15\%$. In the investigated parameter field, it was demonstrated that the most significant influence on the density is exerted by the laser power, followed by the scan speed. High densities tend to be achieved by low scanning speeds and high laser powers. The requirement of high energy densities is mainly related to the material-inherent properties of Al alloys. On the one hand, Al shows a high reflectivity of up to 91% in the range of the Yb fiber laser wavelength of 1070 nm [28]. With increasing temperature, the reflectivity decreases significantly to a value of 60% at temperatures slightly below the melting point [29]. In addition, Al has a high thermal conductivity of 237 W/mK, which causes rapid heat dissipation and thus also requires a higher energy density during fabrication [30]. Both laser power and scan speed influence the grain size, the solidification morphology, and the volatilization of alloy constituents with increasing temperature, as cooling rate tends to decrease with decreasing scan speed, while high laser power increases the thermal gradient and the melt temperature [30]. Since the melt becomes less viscous with increasing temperature, this has a positive effect on the susceptibility to hot cracking, since cracks that occur are efficiently backfilled with melt [30]. It is known that lower scan velocities reduce the susceptibility to cracking in AlCuMgZr alloys [18]. Furthermore, there is a tendency towards larger hatch distances. This trend contradicts literature, as the risk of forming gaps between adjacent melt tracks, leading to insufficient metallurgical bonding between layers and lack-of-fusion defects, is higher for larger hatch distances [4]. A low hatch distance increases the energy per volume introduced into the part, thus increasing the wettability of the liquid melt. However, in the case of the studied alloy, the trend towards larger hatch distance can be explained by heat accumulations in the melt pool and, consequently, the evaporation of volatile alloying

elements for too low hatch distances, which then are reflected in higher porosity [31].

Particular emphasis should be placed on the crack-free microstructure since interdendritic hot cracking is the biggest problem with LPBF-manufactured 2618 [15,32]. It is known from the literature that the crack susceptibility is most pronounced at a Cu content of 1.5–3.0 wt% and an Mg content of 1.0–2.5 wt% [33]. The Cu- and Mg-content of the studied alloy of 2.36 ± 0.10 wt% and 1.95 ± 0.02 wt%, respectively, is within this range, as is the majority of non-weldable 2xxx series Al alloys. The reason for the formation of solidification and liquation cracks is the pronounced segregation of low-melting compounds with high viscosity on the GBs, which can often be observed in alloys with a high solidification interval. Elemental segregation of low melting point compounds during solidification leads to the formation of a film on the GBs as well as the interdendritic region. Under tensile stresses/strains due to solidification shrinkage and thermal contraction, interdendritic cracks form, often spanning over multiple grains or layers. Owing to an excessively viscous residual melt or an insufficient volume of residual melt, these cracks cannot be backfilled [5,33]. A known possibility to reduce the susceptibility to hot cracking in LPBF and casting processes is the addition of Si as in the well-known near-eutectic alloys AlSi_{12} and $\text{AlSi}_{10}\text{Mg}$, as Si reduces the viscosity of the melt, the solidification interval, and the thermal contraction, as well as increases the wettability [34]. However, the amount of 0.24 ± 0.01 wt% Si in the present alloy is presumably too low to cause a significant reduction in hot cracking susceptibility. Hot cracking susceptibility increases significantly for Si contents up to 1 wt%, to the point where at about 4 wt%, it decreases again [35]. Furthermore, the hot cracking susceptibility can be reduced by adding Sc and/or Zr, which alters the solidification morphology from dendritic towards equiaxed for low solidification front velocities [18]. This is due to the formation of coherent Al_3Sc or Al_3Zr precipitates, which act as inoculants for the α -Al grains. This effect has been comprehensively studied e.g. for the two commercial Zr/Sc modified alloys Addalloy™ and Scalmaalloy®, which are characterized by a crack-free bimodal microstructure of fine equiaxed and coarse columnar grains [11,36,37]. A similar grain refinement mechanism could be demonstrated, for example, by adding TiB_2 to 2618 [38]. The fine, equiaxed α -Al grains, which form around the primary coherent L_{12} - Al_3Zr precipitates, are free to move in the still liquid melt. The mobility of these equiaxed grains is believed to be responsible for relieving generated stresses by translational and rotational movement. The same applies to the larger, equiaxed grains formed in the last stage of melt pool solidification. The solidification front velocity, exponentially increasing from bottom to top of the melt pools, typically exceeds 10^3 mm/s in LPBF [39]. At solidification front velocities of 10^1 – 10^2 mm/s, solute trapping prevents the L_{12} - Al_3Zr formation and leads to supersaturation of Zr into the matrix phase, which in turn does no longer effect grain refinement [36]. However, since high solidification front velocities lead to the formation of

equiaxed grains according to classic solidification theory, the grain refinement effect is not necessary for crack prevention in the later solidification process. In the less mobile columnar-dendritic region, which solidifies chronologically between the two equiaxed grain regions, sufficient low-melting, low viscous eutectic GB phase is present to fill stress cracks and thus to prevent crack formation and propagation. It is assumed that this precipitation network on the GBs also hinders the growth of long columnar grains in the L_{12} - Al_3Zr -free grain region [22]. Moreover, it is known from the laser welding process for 5xxx and 6xxx alloys that the hot cracking susceptibility can be reduced by increasing the laser power as well as reducing the scan speed due to an increase in melt viscosity at higher temperatures. The same trend was found in our alloy [40].

The parameter optimized sample shows a high density of $99.93 \pm 0.02\%$. The few 10–25 μm sized, circularly shaped pores in the cross-sections are characteristic of gas pores. They form by evaporation or sublimation of components with a high vapor pressure due to the process-intrinsic high temperatures of over 2000 °C. Due to the rapid solidification, the gas bubbles are trapped in the consolidated part and remain as pores. Since Mg is the most volatile alloying element in the alloy and a decrease from $1.95 \pm 0.02 \text{ wt}\%$ in the powder to $1.55 \pm 0.03 \text{ wt}\%$ in the component can be observed, the present porosity can be attributed to the evaporation of 0.4 wt% Mg. This important element not only serves in the present alloy for solid solution strengthening of the Al grains, but it is also necessary for the formation of strengthening precipitates (such as $S\text{-}Al_2CuMg$, Mg_2Si). Since this loss of Mg was anticipated when determining the alloy composition, the Mg content of the alloy is in the range of commercial 2618 with 1.20–1.80 wt% and is not too low to compromise the precipitation formation.

The microhardness is averaging $1360 \pm 74 \text{ MPa}$ with an indentation modulus of $94 \pm 3 \text{ GPa}$. Unmodified 2618 and other Al-Cu-Mg based alloys, such as 2024, exhibit as-built hardness values of $1020 \pm 10 \text{ MPa}$ and 1089 MPa , respectively [41,42]. The two commercially available high-strength 5xxx series alloys Addalloy™ and Scalmalloy®, adapted to the LPBF process, show hardness values of $961 \pm 33 \text{ MPa}$ and 1030 MPa , respectively [11,43]. The exceptionally high hardness values of our alloy result from the same L_{12} - $Al_3(Sc,Zr)$ induced GB strengthening used in the latter alloys, combined with the precipitation strengthening characteristic for 2xxx series. Thus, the developed alloy represents a combination of 2xxx series alloys and the 5xxx series alloys adapted to LPBF, not only in terms of chemical composition, but also in terms of mechanical performance.

5.2. Microstructure and precipitate formation

Once the laser has melted the powder, solidification of the Al_3Zr precipitates at the edge of the melt pool begins at a temperature of 975 °C and ends at 634 °C. The specified temperature intervals of the respective phases refer to the Scheil-Gulliver calculations performed by Thermo-Calc®, Fig. 1a. The solidification front velocity is initially slow and gives the Al_3Zr precipitates enough time to nucleate and grow homogeneously. This is reflected in SEM and STEM images by a band, more or less thick, of 50–75 nm large L_{12} - Al_3Zr precipitates at the melt pool boundary. The nucleation of primary L_{12} - Al_3Zr occurs through the formation of a stable crystallization nucleus of critical size in regions with elevated local Zr concentrations and is favored by the initially slow solidification front velocity, as there is sufficient time for nucleation and growth. The grain refining effect of the L_{12} precipitates, which are not homogeneously distributed in the melt pool due to concentration differences, leads to an irregular melt pool geometry which often does not correspond to the hemispherical shape typically observed in the transverse section of conduction mode LPBF. Hence, the melt pool shape is not defined by the conduction of latent heat along the steepest temperature gradient but the formation of L_{12} - Al_3Zr nuclei inducing α -Al crystallization,

consequently leading to a 10–20 μm thick band of equiaxed, 0.3–1.6 μm sized α -Al grains at the melt pool boundaries.

According to XRD measurements, the Al_3Zr phase is present as metastable L_{12} (0.2 wt%) as well as stable DO_{23} (3.9 wt%). The stable DO_{23} phase is incoherent to the matrix and thus does not contribute to grain refinement. However, previous studies of Zr-modified Al alloys have shown that the majority of Al_3Zr is present as the metastable L_{12} rather than the stable DO_{23} configuration [11,22]. Although the phase analysis shows 3.9 wt% DO_{23} , the cross-sections examined by SEM show only very few 5–10 μm long, 0.1–0.25 μm wide DO_{23} precipitates; no DO_{23} was detected in the lamella examined by STEM. XRD evaluates the total amount of Al_3Zr (L_{12} + DO_{23}) in the material as 4.1 wt%, which translates into 2.17 wt% overall Zr within the alloy. It is thus exceeding the $1.71 \pm 0.05 \text{ wt}\%$ Zr determined by ICP-OES, Table 1. Besides, STEM-EDS shows Zr dissolved in the solid solution, leading to the conclusion that the amount of DO_{23} from XRD might be significantly overestimated. This may be due to a peak overlap of L_{12} with DO_{23} as well as with Al_5FeNi , which makes it difficult to quantify these phases accurately.

In the further course of solidification, the α -Al matrix phase forms over the solidification interval 634–427 °C and establishes a trimodal solidification morphology. (i) Heterogeneous nucleation on the numerous 50–100 nm-sized coherent L_{12} - Al_3Zr precipitates at the melt pool edge forms a 5–20 μm wide band of 300–1600 nm α -Al grains around the L_{12} - Al_3Zr precipitates. Subsequently, the solidification front velocity increases until partial solute trapping suppresses the formation of the L_{12} nuclei. (ii) Epitaxial growth of a band of 5–15 μm long, 1–3 μm large columnar-dendritic grains then follows. The (low) anisotropy of this band compared to the rest of the microstructure is responsible for the weak texture in $\{011\} < 001 >$ direction. (iii) For the remaining part, the melt pool consists of coarser, equiaxed grains. The decreasing thermal gradient ahead of the solidification front with continued solidification, together with the increase in liquidus temperature by solute partitioning, increases the constitutional supercooling sufficiently to allow the homogeneous nucleation of 1–3 μm -sized, equiaxed α -Al ahead of the solidification front. Complete solute trapping by a very high solidification front velocity prevents the formation of L_{12} - Al_3Zr precipitates in this region. The α -Al lattice parameter is slightly increased at 4.056 Å compared to pure aluminum at 4.048 Å, Table 2, indicating the distortion of the lattice by intercalated atoms forming a solid solution [44]. The lattice parameter is slightly lower than in binary AlMg alloys with a similar Mg content, which indicates other alloying elements in solid solution [45,46]. While, for example, Cu, Ni, and Zn decrease the lattice parameter, it is significantly increased by Mg, which has a solubility up to 15 at% at 450 °C [47]. Thus, Mg and Zr seem to be responsible for the 0.2% larger lattice parameter, although other alloying elements (mainly Fe, Ni) in the solid solution concurrently decrease the lattice parameter. Compared to the feedstock powder, the chemical analysis revealed that the content of Mg, the lowest-melting element of the alloy, decreased by 0.4 wt% from $1.95 \pm 0.02 \text{ wt}\%$ in the powder down to $1.55 \pm 0.03 \text{ wt}\%$ in the consolidated parts and is thus, as planned, within the range of the nominal Mg content of 2618, Table 1. It is also noticeable that the actual Zr content in the powder of $1.71 \pm 0.05 \text{ wt}\%$ is slightly lower than the nominal Zr range of 1.80–2.00 wt%, but remains within the range of previously tested Zr contents for crack prevention [11,22,48]. Furthermore, minor contamination of the feedstock powder with $0.05 \pm 0.001 \text{ wt}\%$ Sn could be observed.

Shortly after the start of solidification of the matrix phase, various precipitates begin to form on the grain boundaries. Starting at a temperature of 629 °C up to 550 °C, Fig. 1a, the formation of the eutectic $(Al,Cu)_9FeNi$ (11.2 wt%) begins. This phase accounts for the largest proportion of precipitates formed. Within the melt pools, but not in the fine-equiaxed grain zone, the phase is present in a blocky shape on the GBs. This corresponds to the shape reported in the

literature [49,50]. In the fine-equiaxed, remelted zone of subsequent laser passes, it is found agglomerated in the form of small, 10–50 nm-sized balls on the GBs, Fig. 6b,c.

It is assumed that the eutectic at GBs partially dissolves. With progressing solidification front, those ball-shaped fragments are rejected into the GB region. It can be expected that the metastable shape is transformed into the stable needle or flake shape by Ostwald ripening during subsequent heat treatment. As Al_9FeNi has an Al_9Co_2 structure type (space group $\text{P2}_1/\text{c}$, 22 atoms per unit cell), the present $(\text{Al,Cu})_9\text{FeNi}$ phase shows slightly different lattice parameters as compared to literature due to stretching in each spatial direction [51]. The solubility of alloying elements in Al_9FeNi has already been shown for the substitution of Fe by Ni as well as Ni by Cu [52–54]. A solubility of Cu is plausible and can be explained based on the rules established by Hume-Rothery. Due to the different atomic radii of 0.128 nm for Cu and 0.143 nm for Al (atomic misfit of +10.5%), the low chemical affinity based on the small electronegativity difference (2.2 for Cu and 1.5 for Al, respectively) as well as a small valence electron difference (one for Cu and three for Al, respectively), substitutional or interstitial incorporation of Cu can be expected. Noteworthy, Thermo-Calc® does not consider the solubility of Cu in Al_9FeNi , leading to the calculated residual melt being more rich in Cu than in reality. This can affect the formation of subsequently precipitated phases.

In the temperature range 553–468 °C, Fig. 1a, the Mg_2Si (0.5 wt%) phase is formed, which due to segregation effects is found on the GBs, and found with a solubility of Sn. Mg is also found with O, presumably forming small amounts of spinel MgAl_2O_4 , Fig. 6. The Mg_2Si precipitates are about 100 nm in diameter and are occasionally visible sandwiched between the Al_9FeNi precipitates. In as-cast 2618, the occurrence of Mg_2Si precipitates was reported as well [55]. In the temperature range of 482–468 °C, the formation of $\text{S-Al}_2\text{CuMg}$ joins in. Although $\text{S-Al}_2\text{CuMg}$ (0.2 wt%) was identified by XRD, Fig. 4, the phase could not be found in the investigated lamella by STEM. Yet, literature on casted Al-Cu-Mg(-Fe-Ni) as well as LPBF fabricated Al-Cu-Mg alloys could prove the presence of $\text{S-Al}_2\text{CuMg}$, indicating its possible presence in the examined alloy [22,25,56]. Since $\text{S-Al}_2\text{CuMg}$ forms within the residual 1.5 mol.% of melt, segregation effects should lead to its presence on the GBs. Similarly, the formation of CuAl , which forms under equilibrium conditions at Cu-contents > 48.7 wt%, is not calculated by Thermo-Calc®.

Since 2618 and Zr-containing alloys undergo a significant strength increase by either Mg_2Si and Al_2CuMg and secondary, nanometric $\text{L}_{12}\text{-Al}_3\text{Zr}$ precipitation hardening, respectively, a subsequent modified T6 or T61 heat treatment to improve the mechanical performance will be the focus of future work.

6. Conclusions

This work investigates the processability of a novel, modified 2618 alloy by LPBF, with a focus on the microstructure and precipitate formation. The 2xxx alloy grade is classified as non-weldable, mainly due to its high Cu and Mg content. By adding Zr, along with process parameter optimization, hot cracking can be successfully suppressed and a fine-grained microstructure can be achieved, with parts exhibiting high density. By adjusting the Mg content, the base chemical composition corresponds exactly to that of traditionally produced 2618. In-depth analyses of the microstructure and phase formation provide better insight into the material behavior of 2xxx alloys during rapid solidification and lay the foundation for further heat treatment studies. The knowledge gained can significantly advance the commercialization of a 2xxx series alloy tailored to LPBF. In detail, the following conclusions were reached:

- (1) Consolidated parts show no cracks and a high relative density of 99.9% or more. The most significant parameter for density

optimization is laser power. The chemical composition is within the industrial specifications for 2618, plus Zr.

- (2) The trimodal microstructure consists of very fine equiaxed (~0.5 μm), columnar-dendritic (5–15 μm long, 1–3 μm wide) and coarser equiaxed grains (1–3 μm) and shows very weak texture. Within the fine-equiaxed grains, abundant metastable cuboidal $\text{L}_{12}\text{-Al}_3\text{Zr}$ are found, but are not present in the other regions, presumably due to solute trapping. Stable $\text{DO}_{23}\text{-Al}_3\text{Zr}$ can be detected sporadically.
- (3) Several types of precipitates are present on the grain boundaries due to segregation, such as $(\text{Al,Cu})_9\text{FeNi}$, Mg_2Si , Al_2CuMg , and AlCu . These contribute to the fine-grained microstructure by hindering grain growth and contribute to strength enhancement.
- (4) The microhardness is 1360 ± 74 MPa with an indentation modulus of 94 ± 3 GPa. The developed alloy is harder than conventionally produced 2xxx alloys (e.g. 2024, 2618) as well as the two commercially available alloys adapted to the LPBF process, Scalmanloy® and Addalloy™.

CRediT authorship contribution statement

Marvin Schuster: Conceptualization, Methodology, Investigation, Validation, Formal analysis, Visualization, Writing – original draft. **Anthony De Luca:** Conceptualization, Methodology, Investigation, Visualization, Writing – review & editing, Supervision. **Remo Widmer:** Investigation. **Xavier Maeder:** Investigation. **Christian Leinenbach:** Conceptualization, Writing – review & editing, Supervision, Project administration, Funding acquisition.

Data Availability

The data of this work will be made available upon reasonable request.

Declaration of Competing Interest

The authors declare that they have no known competing financial interests or personal relationships that could have appeared to influence the work reported in this paper.

Acknowledgments

The research leading to this work was funded by the Swiss Innovation Agency (Innosuisse) under project Nr. 27436.1 PFNM-NM.

Appendix A. Supporting information

Supplementary data associated with this article can be found in the online version at doi:10.1016/j.jallcom.2022.165346.

References

- [1] W.E. Frazier, Metal additive manufacturing: a review, *J. Mater. Eng. Perform.* 23 (2014) 1917–1928, <https://doi.org/10.1007/s11665-014-0958-z>
- [2] W. Meiners, Direktes selektives Laser-Sintern einkomponentiger metallischer Werkstoffe, *Als Ms. Gedr Shak. Aachen* (1999).
- [3] D. Buchbinder, H. Schleifenbaum, S. Heidrich, W. Meiners, J. Bültmann, High power selective laser melting (HP SLM) of aluminum parts, *Phys. Procedia* 12 (2011) 271–278, <https://doi.org/10.1016/j.phpro.2011.03.035>
- [4] N.T. Aboulkhair, N.M. Everitt, I. Ashcroft, C. Tuck, Reducing porosity in AlSi10Mg parts processed by selective laser melting, *Addit. Manuf.* 1–4 (2014) 77–86, <https://doi.org/10.1016/j.addma.2014.08.001>
- [5] J.H. Martin, B.D. Yahata, J.M. Hundley, J.A. Mayer, T.A. Schaedler, T.M. Pollock, 3D printing of high-strength aluminium alloys, *Nature* 549 (2017) 365–369, <https://doi.org/10.1038/nature23894>
- [6] D. Fabregue, Microstructure et fissuration à chaud lors du soudage laser d'alliages d'aluminium 6000, phdthesis, Institut National Polytechnique de Grenoble - INPG, 2004. (<https://tel.archives-ouvertes.fr/tel-00370426>) (accessed January 18, 2022).
- [7] W. Stopyra, K. Gruber, I. Smolina, T. Kurzynowski, B. Kuźnicka, Laser powder bed fusion of AA7075 alloy: influence of process parameters on porosity and hot

- cracking, Addit. Manuf. 35 (2020) 101270, <https://doi.org/10.1016/j.addma.2020.101270>
- [8] L. Thijs, K. Kempen, J.-P. Kruth, J. Van Humbeeck, Fine-structured aluminium products with controllable texture by selective laser melting of pre-alloyed AlSi10Mg powder, Acta Mater. 61 (2013) 1809–1819, <https://doi.org/10.1016/j.actamat.2012.11.052>
 - [9] K.G. Prashanth, S. Scudino, J. Eckert, Defining the tensile properties of Al-12Si parts produced by selective laser melting, Acta Mater. 126 (2017) 25–35, <https://doi.org/10.1016/j.actamat.2016.12.044>
 - [10] Y.J. Liu, Z. Liu, Y. Jiang, G.W. Wang, Y. Yang, L.C. Zhang, Gradient in microstructure and mechanical property of selective laser melted AlSi10Mg, J. Alloy. Compd. 735 (2018) 1414–1421, <https://doi.org/10.1016/j.jallcom.2017.11.020>
 - [11] J.R. Croteau, S. Griffiths, M.D. Russell, C. Leinenbach, C. Kenel, V. Jansen, D.N. Seidman, D.C. Dunand, N.Q. Vo, Microstructure and mechanical properties of Al-Mg-Zr alloys processed by selective laser melting, Acta Mater. 153 (2018) 35–44, <https://doi.org/10.1016/j.actamat.2018.04.053>
 - [12] A.B. Spierings, K. Dawson, M. Voegtlin, F. Palm, P.J. Uggowitzer, Microstructure and mechanical properties of as-processed scandium-modified aluminium using selective laser melting, CIRP Ann. 65 (2016) 213–216, <https://doi.org/10.1016/j.cirp.2016.04.057>
 - [13] V.S. Zolotarevsky, N.A. Belov, M.V. Glazoff, Chapter one - Alloying Elements and Dopants: Phase Diagrams, in: V.S. Zolotarevsky, N.A. Belov, M.V. Glazoff (Eds.), Casting Aluminum Alloys, Elsevier, Amsterdam, 2007, pp. 1–93, <https://doi.org/10.1016/B978-0-08045370-5.50003-1>
 - [14] S.Z. Uddin, L.E. Murr, C.A. Terrazas, P. Morton, D.A. Roberson, R.B. Wicker, Processing and characterization of crack-free aluminum 6061 using high-temperature heating in laser powder bed fusion additive manufacturing, Addit. Manuf. 22 (2018) 405–415, <https://doi.org/10.1016/j.addma.2018.05.047>
 - [15] L. Pantelejev, D. Koutny, D. Palousek, J. Kaiser, Mechanical and microstructural properties of 2618 Al-alloy processed by SLM remelting strategy, MSF 891 (2017) 343–349, <https://doi.org/10.4028/www.scientific.net/MSF.891.343>
 - [16] S.C. Wang, M.J. Starink, Two types of S phase precipitates in Al-Cu-Mg alloys, Acta Mater. 55 (2007) 933–941, <https://doi.org/10.1016/j.actamat.2006.09.015>
 - [17] A. Aversa, G. Marchese, A. Saboori, E. Bassini, D. Manfredi, S. Biamino, D. Ugues, P. Fino, M. Lombardi, New aluminum alloys specifically designed for laser powder bed fusion: a review, Materials 12 (2019) 1007, <https://doi.org/10.3390/ma12071007>
 - [18] H. Zhang, H. Zhu, X. Nie, J. Yin, Z. Hu, X. Zeng, Effect of Zirconium addition on crack, microstructure and mechanical behavior of selective laser melted Al-Cu-Mg alloy, Scr. Mater. 134 (2017) 6–10, <https://doi.org/10.1016/j.scriptamat.2017.02.036>
 - [19] C. Doñate-Buendia, P. Kürnsteiner, F. Stern, M.B. Wilms, R. Streubel, I.M. Kusoglu, J. Tenkamp, E. Bruder, N. Pirch, S. Barcikowski, K. Durst, J.H. Schleifenbaum, F. Walther, B. Gault, B. Gökce, Microstructure formation and mechanical properties of ODS steels built by laser additive manufacturing of nanoparticle coated iron-chromium powders, Acta Mater. 206 (2021) 116566, <https://doi.org/10.1016/j.actamat.2020.116566>
 - [20] G. Li, E. Brodu, J. Soete, H. Wei, T. Liu, T. Yang, W. Liao, K. Vanmeensel, Exploiting the rapid solidification potential of laser powder bed fusion in high strength and crack-free Al-Cu-Mg-Mn-Zr alloys, Addit. Manuf. 47 (2021) 102210, <https://doi.org/10.1016/j.addma.2021.102210>
 - [21] K. Siebertz, D. van Bebber, T. Hochkirchen, Statistische Versuchsplanung, Springer Berlin Heidelberg, Berlin, Heidelberg, 2017, <https://doi.org/10.1007/978-3-662-55743-3>
 - [22] M. Schuster, A. De Luca, A. Mathur, E. Hosseini, C. Leinenbach, Precipitation in a 2xxx series Al-Cu-Mg-Zr alloy fabricated by laser powder bed fusion, Mater. Des. 211 (2021) 110131, <https://doi.org/10.1016/j.matdes.2021.110131>
 - [23] J.T. McKeown, A.K. Kulovits, C. Liu, K. Zweigacker, B.W. Reed, T. LaGrange, J.M.K. Wiezorek, G.H. Campbell, In situ transmission electron microscopy of crystal growth-mode transitions during rapid solidification of a hypoeutectic Al-Cu alloy, Acta Mater. 65 (2014) 56–68, <https://doi.org/10.1016/j.actamat.2013.11.046>
 - [24] B. Hu, S. Qin, Y. Du, Z. Li, Q. Wang, Thermodynamic description of the Al-Fe-Mg-Ni-Si and Al-Cu-Fe-Mg-Ni quinary systems and its application to solidification simulation, J. Ph. Equilib. Diffus. 36 (2015) 333–349, <https://doi.org/10.1007/s11669-015-0388-0>
 - [25] N.A. Belov, D.G. Eskin, A.A. Aksenov, Multicomponent Phase Diagrams: Applications for Commercial Aluminum Alloys, Elsevier, 2005.
 - [26] A.B. Spierings, K. Dawson, P. Dumitraschkewitz, S. Pogatscher, K. Wegener, Microstructure characterization of SLM-processed Al-Mg-Sc-Zr alloy in the heat treated and HIPed condition, Addit. Manuf. 20 (2018) 173–181, <https://doi.org/10.1016/j.addma.2017.12.011>
 - [27] Y. Du, S. Liu, K. Chang, B. Hu, M. Bu, W. Jie, W. Huang, J. Wang, Thermodynamic modelling and Gulliver-Scheil simulation of multi-component Al alloys, IOP Conf. Ser. Mater. Sci. Eng. 27 (2012) 012082, <https://doi.org/10.1088/1757-899X/27/1/012082>
 - [28] J. Zhang, B. Song, Q. Wei, D. Bourell, Y. Shi, A review of selective laser melting of aluminum alloys: processing, microstructure, property and developing trends, J. Mater. Sci. Technol. 35 (2019) 270–284, <https://doi.org/10.1016/j.jmst.2018.09.004>
 - [29] K. Ujihara, Reflectivity of metals at high temperatures, J. Appl. Phys. 43 (1972) 2376–2383, <https://doi.org/10.1063/1.1661506>
 - [30] Y. Li, D. Gu, Parametric analysis of thermal behavior during selective laser melting additive manufacturing of aluminum alloy powder, Mater. Des. 63 (2014) 856–867, <https://doi.org/10.1016/j.matdes.2014.07.006>
 - [31] Y. Pupo, J. Delgado, L. Serenó, J. Ciurana, Scanning space analysis in selective laser melting for CoCrMo powder, Procedia Eng. 63 (2013) 370–378, <https://doi.org/10.1016/j.proeng.2013.08.228>
 - [32] D. Koutny, D. Palousek, L. Pantelejev, C. Hoeller, R. Pichler, L. Tesicky, J. Kaiser, Influence of scanning strategies on processing of aluminum alloy EN AW 2618 using selective laser melting, Materials 11 (2018) 298, <https://doi.org/10.3390/ma11020298>
 - [33] C. Galy, E. Le Guen, E. Lacoste, C. Arvieu, Main defects observed in aluminum alloy parts produced by SLM: from causes to consequences, Addit. Manuf. 22 (2018) 165–175, <https://doi.org/10.1016/j.addma.2018.05.005>
 - [34] R. Cornell, H.K.D.H. Bhadeshia, Aluminium-Silicon Casting Alloys, (2021). (<https://www.phase-trans.msm.cam.ac.uk/abstracts/M7-8.html>) (Accessed 19 March, 2021).
 - [35] H. Hyer, L. Zhou, A. Mehta, S. Park, T. Huynh, S. Song, Y. Bai, K. Cho, B. McWilliams, Y. Sohn, Composition-dependent solidification cracking of aluminum-silicon alloys during laser powder bed fusion, Acta Mater. 208 (2021) 116698, <https://doi.org/10.1016/j.actamat.2021.116698>
 - [36] S. Griffiths, M.D. Russell, J. Croteau, N.Q. Vo, D.C. Dunand, C. Leinenbach, Effect of laser rescanning on the grain microstructure of a selective laser melted Al-Mg-Zr alloy, Mater. Charact. (2018), <https://doi.org/10.1016/j.matchar.2018.03.033>
 - [37] K. Schmidtke, F. Palm, A. Hawkins, C. Emmelmann, Process and mechanical properties: applicability of a scandium modified Al-alloy for laser additive manufacturing, Phys. Procedia 12 (2011) 369–374, <https://doi.org/10.1016/j.phpro.2011.03.047>
 - [38] F. Beilelli, R. Casati, F. Larini, M. Riccio, M. Vedani, Investigation on two Ti-B-reinforced Al alloys for laser powder bed fusion, Mater. Sci. Eng.: A 808 (2021) 140944, <https://doi.org/10.1016/j.msea.2021.140944>
 - [39] D. Wang, C. Song, Y. Yang, Y. Bai, Investigation of crystal growth mechanism during selective laser melting and mechanical property characterization of 316L stainless steel parts, Mater. Des. 100 (2016) 291–299, <https://doi.org/10.1016/j.matdes.2016.03.111>
 - [40] J.M. Sánchez-Amaya, T. Delgado, L. González-Rovira, F.J. Botana, Laser welding of aluminium alloys 5083 and 6082 under conduction regime, Appl. Surf. Sci. 255 (2009) 9512–9521, <https://doi.org/10.1016/j.apsusc.2009.07.081>
 - [41] R. Casati, J.N. Lemke, A.Z. Alarcon, M. Vedani, Aging behavior of high-strength Al Alloy 2618 produced by selective laser melting, Metall. Mater. Trans. A 48 (2017) 575–579, <https://doi.org/10.1007/s11661-016-3883-y>
 - [42] H. Zhang, H. Zhu, T. Qi, Z. Hu, X. Zeng, Selective laser melting of high strength Al-Cu-Mg alloys: processing, microstructure and mechanical properties, Mater. Sci. Eng.: A 656 (2016) 47–54, <https://doi.org/10.1016/j.msea.2015.12.101>
 - [43] D. Koutny, D. Skulina, L. Pantelejev, D. Palousek, B. Lenczowski, F. Palm, A. Nick, Processing of Al-Sc aluminum alloy using SLM technology, Procedia CIRP 74 (2018) 44–48, <https://doi.org/10.1016/j.procir.2018.08.027>
 - [44] M. Morinaga, 11 - Local Lattice Strains Around Alloying Elements in Metals, in: M. Morinaga (Ed.), A Quantum Approach to Alloy Design, Elsevier, 2019, pp. 221–260, <https://doi.org/10.1016/B978-0-12-814706-1.00011-X>
 - [45] J. Gubicza, M. Kassem, G. Ribárik, T. Ungár, The microstructure of mechanically alloyed Al-Mg determined by X-ray diffraction peak profile analysis, Mater. Sci. Eng.: A 372 (2004) 115–122, <https://doi.org/10.1016/j.msea.2003.12.016>
 - [46] Z. Li, B. Xiong, Y. Zhang, X. Li, B. Zhu, H. Liu, F. Wang, P. Li, ICAA13, H. Weiland, A.D. Rollett, W.A. Cassada (Eds.), X-Ray Diffraction Study on Lattice Constant of Supersaturated Solid Solution for Al Based Binary Alloys and Selected Al-Zn-Mg-Cu Alloys, Springer International Publishing, Cham, Pittsburgh, 2016, pp. 1295–1300, https://doi.org/10.1007/978-3-319-48761-8_199 ICAA13.
 - [47] D. Shin, S. Roy, T.R. Watkins, A. Shyam, Lattice mismatch modeling of aluminum alloys, Comput. Mater. Sci. 138 (2017) 149–159, <https://doi.org/10.1016/j.commatsci.2017.06.021>
 - [48] Y. Wang, X. Lin, N. Kang, Z. Wang, Y. Liu, W. Huang, Influence of post-heat treatment on the microstructure and mechanical properties of Al-Cu-Mg-Zr alloy manufactured by selective laser melting, J. Mater. Sci. Technol. (2021), <https://doi.org/10.1016/j.jmst.2021.09.036>
 - [49] A.D. Setyawan, D.V. Louzguine, K. Sasamori, H.M. Kimura, S. Ranganathan, A. Inoue, Phase composition and transformation behavior of readily solidified Al-Ni-Fe alloys in α -Al-decagonal phase region, J. Alloy. Compd. 399 (2005) 132–138, <https://doi.org/10.1016/j.jallcom.2005.03.020>
 - [50] F. Meng, Y. Wu, K. Hu, Y. Li, Q. Sun, X. Liu, Evolution and strengthening effects of the heat-resistant phases in Al-Si Piston alloys with Different Fe/Ni ratios, Materials 12 (2019) 2506, <https://doi.org/10.3390/ma12162506>
 - [51] Z. Bian, Y. Liu, S. Dai, Z. Chen, M. Wang, D. Chen, H. Wang, Regulating microstructures and mechanical properties of Al-Fe-Ni alloys, Prog. Nat. Sci.: Mater. Int. 30 (2020) 54–62, <https://doi.org/10.1016/j.pnsc.2019.12.006>
 - [52] C.-L. Chen, R.C. Thomson, The combined use of EBSD and EDX analyses for the identification of complex intermetallic phases in multicomponent Al-Si piston alloys, J. Alloy. Compd. 490 (2010) 293–300, <https://doi.org/10.1016/j.jallcom.2009.09.181>
 - [53] M. Warmuzek, Chemical composition of the Ni-containing intermetallic phases in the multicomponent Al alloys, J. Alloy. Compd. 604 (2014) 245–252, <https://doi.org/10.1016/j.jallcom.2014.03.119>
 - [54] A.R. Farkoosh, M. Javidani, M. Hoseini, D. Larouche, M. Pegkulyuz, Phase formation in as-solidified and heat-treated Al-Si-Cu-Mg-Ni alloys: Thermodynamic assessment and experimental investigation for alloy design, J. Alloy. Compd. 551 (2013) 596–606, <https://doi.org/10.1016/j.jallcom.2012.10.182>
 - [55] S. Toschi, E. Balducci, L. Ceschini, E.A. Mortell, A. Morri, M. Di Sabatino, Effect of Zr addition on overaging and tensile behavior of 2618 aluminum alloy, Metals 9 (2019) 130, <https://doi.org/10.3390/met9020130>
 - [56] Y. Wang, X. Lin, N. Kang, Z. Wang, Q. Wang, Y. Liu, W. Huang, Laser powder bed fusion of Zr-modified Al-Cu-Mg alloy: crack-inhibiting, grain refinement, and mechanical properties, Mater. Sci. Eng. A (2022) 142618, <https://doi.org/10.1016/j.msea.2022.142618>